International Journal of Heat and Mass Transfer 190 (2022) 122775

Contents lists available at ScienceDirect

International Journal of Heat and Mass Transfer

journal homepage: www.elsevier.com/locate/hmt

Experimental aerothermal characterization of surface air-cooled oil coolers for turbofan engines

A. Broatch[a], P. Olmeda[a], J. García-Tíscar[a,*], A. Felgueroso[a], M. Chávez-Modena[b], L.M. González[b], M. Gelain[c], A. Couilleaux[c]

[a] CMT – Motores Térmicos, Universitat Politècnica de València, Camino de Vera, Valencia 46022, Spain
[b] ETSIAE – School of Aeronautics, Universidad Politécnica de Madrid, Plaza Cardenal Cisneros 3, Madrid 28040, Spain
[c] Safran Aircraft Engines, Rond-point René Ravaud, Moissy-Cramayel 77550, France

ARTICLE INFO

Article history:
Received 23 November 2021
Revised 23 February 2022
Accepted 6 March 2022

Keywords:
Aero engines
Experimental aerodynamics
Heat exchangers
Turbomachinery
Thermal management
SACOC

ABSTRACT

Thermal management is a major challenge for new generation turbofan aero-engines. One of the most promising heat exchangers are the so-called surface air-cooled oil coolers (SACOCs). In this study, an experimental methodology is proposed and implemented in order to characterize SACOCs mounted in turbofan bypass ducts. Three different SACOC geometries have been characterized under the same nominal operating point, while the actual velocity profile in the bypass was reproduced by means of a distortion screen upstream the test section. The heat exchangers were mounted in counterflow configuration and feature the same fin geometry in the oil side. The three prototypes varied only in the air side, being the first a baseline flat plate, the second a SACOC with standard trapezoidal fins and the third featuring optimized fins designed to reduce the pressure drop. Aerothermal results demonstrated that the effect of the SACOC on the bypass flow was confined to a region about the same height and width of the finned area, avoiding the need of reproducing the whole bypass duct. However, for this reduced-height experimental approach to be valid, we show that the velocity profile needs to be rearranged to match the specific section of the whole bypass. We also demonstrate how the optimized fin geometry achieved a 10% lower friction factor than the standard one at nominal flow conditions while increasing the overall heat transfer coefficient by 5.2%.

1. Introduction

The trend of recent years towards more compact engines in aviation and the use of turbofans with a larger bypass ratio can be explained with the goal of reducing pollutant gases, noise and fuel consumption. All these issues are a major concern in the development of a sustainable aviation industry. Some research programmes, such as Clean Sky [1], have dedicated a great effort to the improvement of aero engines, their related systems and their integration with the airframe.

However, new challenges come across with new generation turbofans. Regarding thermal management, three main aspects need to be considered: the consequence of increasing the size of the fan blades, the shrinking of the engine and the progress of electrification.

On the one hand, the increment in bypass ratios to values over 15:1 provides the ability of augmenting the fuel efficiency by 20 to 25% [2], but the optimal rotational speed of these large fans is incompatible with the typical rotational speed of the turbine that drives them. To solve this issue, a gearbox to reduce the velocity of the fan is installed, a configuration which is often known as 'geared turbofan'. The gearbox needs to be lubricated and kept at reasonable temperatures, but due to the transmitted power, the amount of heat to be evacuated is enormous, even if losses of around 1% [3] are achieved. Per the same reference, common mechanical losses up to 65% full-load, full-speed power can occur in the gearbox. Adequate lubrication will be also a major challenge for future, innovative designs such as CFM's RISE open-rotor configuration, whose target is to achieve a 20% gain in fuel efficiency.

On the other hand, the increment in power produced by the core of the engine has to be also considered for the design of the bearings. Adequate bearing performance can reduce the losses produced during operation, but, similarly to the gearbox, as the power they have to work under is so large, the heat transmitted to the oil

* Corresponding author.
E-mail address: jorgarti@mot.upv.es (J. García-Tíscar).

https://doi.org/10.1016/j.ijheatmasstransfer.2022.122775

as a consequence is substantially higher. In fact, the oil system is not only needed by the bearings as lubricant, but mainly as coolant [4].

Additionally, as electrification and automation advance, the cooling requirements for their proper operation are more demanding. As the size of the engines tends to reduce, the number of heat sinks decrease since the heat can also be dissipated through different engine components, and Van Heerden et al. [5] have considered the integration between engine, airframe and their systems to develop a thermal model that predicts their interactions. Addressing the small size issue, Vankan et al. [6] have developed a graph-based approach to optimize the installation of different engine components inside compact nacelles. Moreover, as fuel efficiency rises, fuel consumption diminishes and therefore, less fuel is available in Fuel-Oil Heat Exchangers (FOHEs), so extra cooling devices such as AOHEs (Air-Oil Heat Exchangers) become even more important.

To overcome these challenges, new generation turbofans have to include an adequate cooling system that enables the proper functioning of the engine in smaller spaces, using the cold bypass flow as a heat sink. This has the additional advantage of re-using that enthalpy in the secondary nozzle. Compact heat exchangers can be classified [7] mainly as plate heat exchangers, plate-fin heat exchangers and printed circuit heat exchangers. Although several studies have considered different fin configurations and performances [8–10], they have been done under low Reynolds numbers.

For the aerospace industry, several companies have proposed many patents [11,12] regarding heat exchangers for ultra-high bypass ratio (UHBR) turbofans. In this sector, the weight is also something to be considered, and Filburn et al. [13] carried out a simplified analysis of a carbon-carbon finned heat exchanger that reduced the weight to a 53% of the original weight of an aluminium heat exchanger. Williams et al. [14] have developed a microchannel heat exchanger to enhance the thermal management in fuel-to-air cooling systems.

Saltzman et al. [15] designed and evaluated an additive manufacturing heat exchanger, that improved the heat removal up to 14%, but almost doubling the pressure drop. It is indeed highly important to consider the effect of the heat exchanger in the pressure drop, since this can affect significantly the engine performance, and Dube et al. [16] have developed a statistical model to predict the pressure drop in the air side of a heat exchanger. In order to accomplish a better performance in terms of heat transfer and/or pressure drop, Bošnjaković et al. [17] added an innovative star-shaped fin and gained a 39.3% of extra heat exchange compared to regular annular fins, with a decrease in mass flow through the exchanger of 23.8%. Zhang et al. [18] were able to reduce the pressure drop by 1/6 approximately using airfoil-shaped fins instead of zigzag channels in a Printed Circuit Heat Exchanger. Another example in pressure drop reduction and heat exchange enhancement can be found in [19], where Gong et al. simulated numerically V-shaped oblique wavy surfaces, changing geometric parameters, to find the optimum configuration for heat transfer and pressure loss, reaching a goodness factor and a Colburn factor increase of 16% and 150%, compared to a flat plate.

Another effect to consider is the fluid-structure interaction in finned heat exchangers. Zhang et al. [20] proved that the larger the fin offset and the thinner the fin is, the greater mechanical and thermal stress they have to withstand.

Focusing on plate-fin heat exchangers located in the bypass of a turbofan, Kim et al. [21] conducted a numerical study validated experimentally with a single-fin heat exchanger in which the aerodynamic and thermodynamic performances were evaluated for different positions of the exchanger. Also Kim et al. [22] continued the study with numerical investigation on the performance of different plate- and pin-fin geometries under similar conditions.

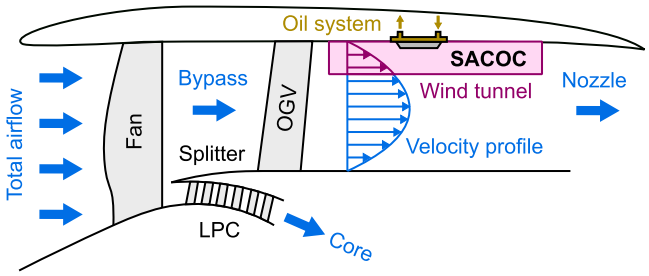

Fig. 1. Configuration considered in this investigation, highlighting the section that is reproduced in the wind tunnel (not to scale).

Villafañe and Paniagua [23] developed an installation at the von Karman Institute for Fluid Dynamics (VKI) that reproduces the typical swirl and velocities in a turbofan splitter (upstream the outlet guide vanes, OGV) and evaluated the aerothermal performance of continuous and interrupted fins. Using the same facility, Sousa et al. [24] performed a thermal analysis using an inverse heat transfer method to analyse the heat extracted from the lubrication system, showing that an adequate heat exchanger can provide up to 76% of the take-off cooling demands of a modern turbofan.

In our investigation, we consider the configuration shown in Fig. 1, where the heat exchanger is placed downstream of the OGV, as in the setup of Kim et al. [21,22]. Such configuration can be found in modern high-bypass-ratio turbofans such as the CFM LEAP-1A and the Rolls-Royce Trent XWB. A major obstacle of the experimental characterization of this arrangement is of course the reproduction of the bypass flow, which requires a very high air mass flow at high speed. Kim et al. [21] tackled this issue with a very narrow wind tunnel that comprised just one fin, mimicking their periodic numerical setup.

A limitation of this approach, however, is that SACOCs are not continuous along the engine periphery — they only typically cover a portion of the circumference. Therefore, it is relevant to analyze the behaviour of the outer fins, which are not subjected to periodic-like conditions. The precise control of the boundary layer growth in very narrow tunnels so that the periodic-like fin experiences completely freestream conditions can also be difficult. This leads to the need to include at least a few fins and a sizeable separation from the lateral walls, as done in the VKI wind tunnel for their splitter-located SACOC configuration.

As implementing this multi-fin approach in our case, including the whole height of the bypass, would render the mass flow requirement excessive, an alternative approach was implemented consisting of the reduced-height wind tunnel depicted in Fig. 1. This same figure however highlights an issue with this approach: if tests were performed in such a reduced-height wind tunnel, the velocity profile would not follow the distribution that the actual bypass duct features in this section. To this end, in our setup a distortion screen is placed upstream the test section so that the flow will not freely develop a flat velocity profile. Instead, it will mimic the actual bypass profile up to the reproduced height, since Gelain et al. [25] recently demonstrated the importance of replicating one-dimensional boundary conditions in order to obtain reliable results in this type of configuration.

The main objective of this paper is to demonstrate such an affordable methodology to experimentally characterize the performance of different geometries of surface air-cooled oil cooler heat exchangers. To this end, the tailored experimental facility is described in the first place and then the experimental campaign is presented, along with the different geometries to be studied, the instrumentation and the data acquisition and reduction procedures. Next, aerothermal results are analyzed focusing on the velocity fields and the pressure drop induced by each geometry, as

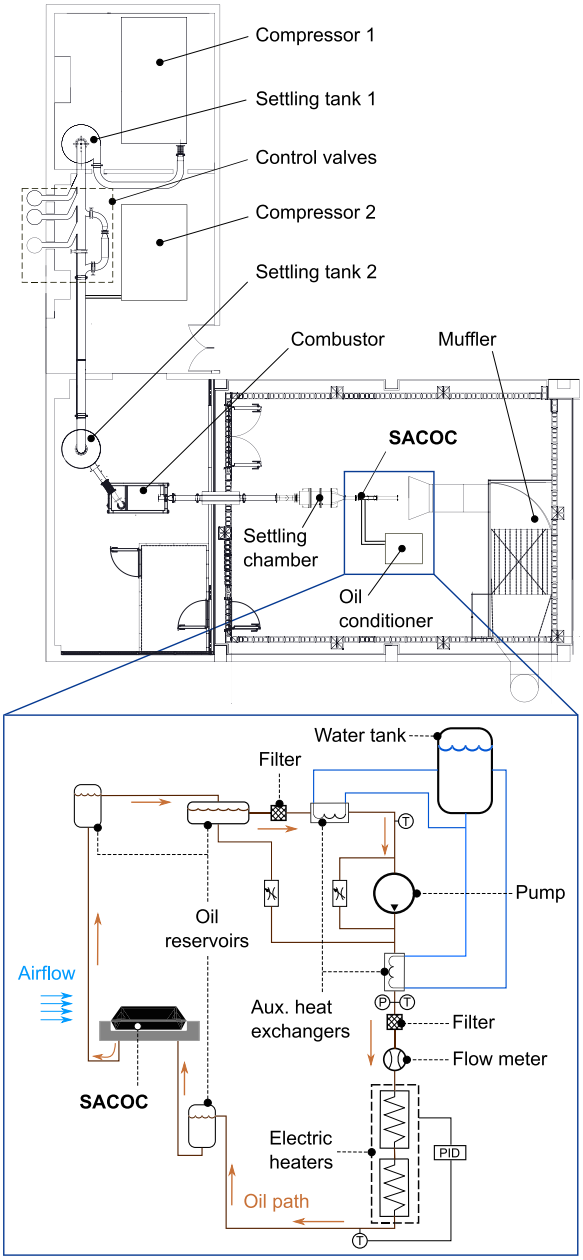

Fig. 2. Facility layout. Schematic of the facility and wind tunnel (top) and detail of the oil conditioning system (bottom).

well as the temperature field at different sections, the wake temperature profiles and the geometry surface temperatures.

2. Experimental facility

2.1. Flow rig

Experiments took place in the main flow rig at 8P laboratory of Universitat Politècnica de València, outlined in Fig. 2. This facility has been designed to carry out aerothermal studies in both automotive [26–28] and aeronautical engineering [29]. A 500 kW two-stage centrifugal compressor is connected in series with a 1 MW Diesel-fired combustion chamber which can heat up to 1000 °C a continuous air mass flow of 1000 kg/h. Bypassing the combustor, the compressor is able to deliver up to 2.15 kg/s of air at 30 °C. In between, two 3 m^3 reservoirs help to deliver a uniform and controlled air mass flow to the test chamber.

In this chamber, an oil conditioning system is installed, composed by a pump that drives the oil through the circuit, a Coriolis mass flow meter to characterize the oil mass flow and an electric heater with two in-series resistors of 2.5 kW each. Several filters and water heat exchangers ensure a proper functioning of all components. A more detailed explanation of the facility and oil conditioner can be found in [30].

2.2. Wind tunnel

A bespoke wind tunnel to characterize the heat exchangers was implemented following the aforementioned approach, as shown in Fig. 3. At the beginning, a settling chamber stagnates the fluid to diminish the flow turbulence and to straighten the streamlines upstream the test section. To do so, a radially-pierced entry based on Purdue University's PETAL settling chamber [31] and two honeycomb panels have been engineered after considering different configurations.

Then, a transition to a squared section with the same shape as the test section drives the flow to a straight duct where the flow develops and reaches the distortion screen. Passing through the screen, the flow undergoes a variation in stagnation pressure induced by differences in porosity designed in such a way that the uniform incoming air profile is transformed into the desired velocity profile, mimicking the actual profile inside the turbofan bypass. Afterwards, a straight section allows the turbulence downstream the distortion screen to settle before the flow reaches the test section.

Immediately upstream and downstream the test section, two piezometric rings composed of 8 static pressure taps (two per wall) are used to determine the pressure drop induced by the model. Finally, after the test section, a straight duct discharges the flow to the ambient of the test chamber, where it is then forced out of the building through a muffler.

2.3. Test section

The test section is a square duct with sides of length H, which will be used to normalize other distances in this paper. Walls are made of borosilicate with the exception of the bottom wall, made of steel. The top wall presents 3 slots to introduce probes in case intrusive measurements are required. In case non intrusive acquisitions take place, the top wall can be substituted by a continuous wall and for thermographic measurements, IR windows transparent in the 0.3 to 13 μm range of the spectrum can be installed. They have a limited field of view, but by installing them in different locations, a complete image of the SACOC can be composed.

Measurements take place in different locations. Pressure drop is characterized with the aforementioned piezometric rings. Total pressures and temperatures are acquired in one section upstream the SACOC, UMS1 (Upstream Measurement Section 1), and two sections downstream it, DMS1 (Downstream Measurement Section 1) and DMS2. To analyse the wake temperature, four thermocouples, TC1, TC2, TC3 and TC4 can be inserted through the bottom wall of the wind tunnel, centered in the span-wise direction. An additional thermocouple, designated TC_{Al}, is inserted from the bottom of the SACOC until it makes contact with the surface. This thermocouple will be used as a reference for thermographic measurements, in order to calibrate the emissivity of the material.

The origin of coordinates is placed on the bottom wall at UMS1, with X following the flow direction, Y facing the upper wall and Z following the right-hand orientation criterion. Values of the positions in the rig are collected in Table 1 and a schematic with the

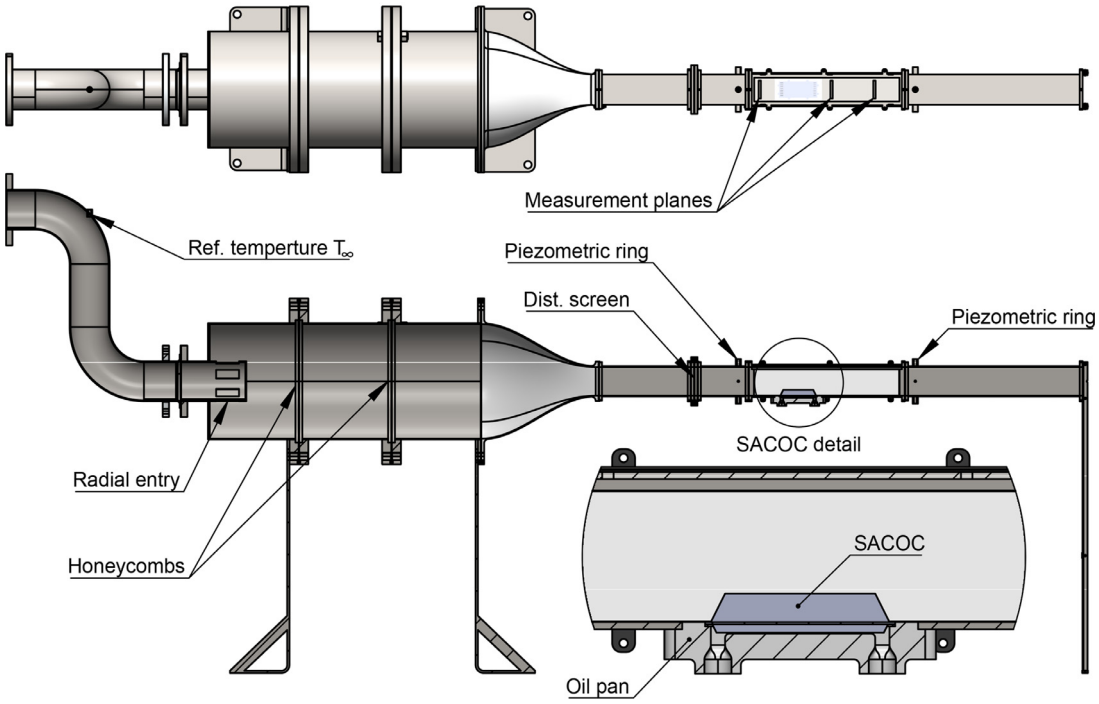

Fig. 3. Drawing of the wind tunnel detailing the installation of the SACOC.

Table 1
Axial location of each relevant section.

Section	X/H [-]
Inlet piezometric ring	−0.65
Inlet test section	−0.36
UMS1	0
Fins leading edge	0.75
TC1	2.4
DMS1	2.5
TC2	2.8
TC3	3.2
TC4	3.6
DMS2	4
Outlet test section	5.11
Outlet piezometric ring	5.4

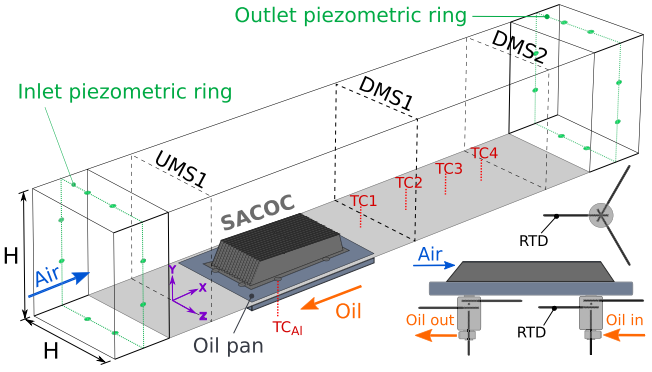

Fig. 4. Sketch of the different instrumentation locations.

different aforementioned locations in the test section can be found in Fig. 4.

In order to provide more general results, through the paper the dimensions are normalized with the test section side H. Other values are used for this normalization, such as the nominal air mass flow $\dot{m}_\infty$, the air freestream static temperature T_∞, the freestream air density ρ_∞ and the maximum freestream air velocity U_∞.

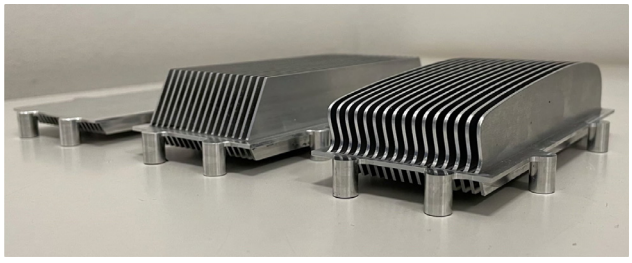

Fig. 5. Photography of the tested SACOCs. From left to right: baseline, standard and optimized geometries.

3. Experimental campaign

3.1. SACOC geometries

For this study, three different geometries are considered: a baseline version, which is a flat plate; a second version, in which a series of standard fins are added to the plate; and a third version, where a topological optimization of the standard fins geometry to reduce the pressure drop was carried out. The three models can be seen in Fig. 5.

3.1.1. Baseline geometry

As a first step, a flat plate heat exchanger geometry was tested in order to obtain the baseline of the experimental setup regarding pressure drop and heat transfer. This allowed a clearer assessment of the performance of the standard-finned SACOC and the optimized fin design.

In the air side, the baseline geometry consists on a flat plate $1.5 \times 10^{-2} H$ thick made of AW7075 T651 aluminium [32]. As with the rest of the geometry, it is attached on top of an oil pan made of ULTEM 1010 [33], which is a thermoplastic that can withstand

high temperatures. The other objective of the plastic oil pan is to thermally isolate the oil as much as possible from the steel wind tunnel, in order to allow heat dissipation to the airstream only through the aluminium exchanger, avoiding conduction losses to the wind tunnel floor.

The surface in contact with the oil has a rectangular shape of 1.25 x 0.5 H with 18 fins with a standard isosceles trapezoidal shape of 0.06 H height. To enhance the heat transfer, the oil circuit is in counterflow, i.e., the oil flows beneath the SACOC in the opposite direction to the airstream above. As it can be seen in Fig. 5, the rectangular base is slightly larger than the oil pan and there are 8 circular stubs to allow a proper attachment from the bottom of the tunnel.

3.1.2. Standard fins

In the second version, a series of isosceles trapezoidal fins are added to the air side. In total, it is provided with 16 fins of $10^{-2}H$ thickness and 0.2 H height, in order to increase the surface area in contact with the air to augment the convection heat exchange [34], and the shape has been chosen as it can be found in current turbofan SACOCs.

In the oil side, the configuration is the same as the baseline, with 18 fins and oil flowing in counterflow, so it is ensured that the variations obtained in the heat exchange are solely related to the air side fins.

3.1.3. Optimized fins

The optimization of the geometric design of the fin shape on the XY plane was performed computationally using a CFD solver in a previous investigation [35]. The process was based on the adjoint method [36,37], using the pressure drop per lateral fin surface area $\Delta p/A_{xy}$ as the objective function while monitoring the heat exchanged to maintain it as constant as possible. This strategy was chosen because in aircraft engines the heat exchange is an operability specification, so there is no intention change it. However, the pressure drop is a loss worth lowering.

The adjoint method is an efficient process to predict the influence of input design geometry, **D**, on some engineering cost function of interest, **L**, which as we already said, in our case, is based on the pressure drop generated by the SACOC divided the lateral fin area, $\Delta p/A_{xy}$. The process is performed in two major steps.

First, a steady state solution, also known as *primal solution*, **Q**, is computed on an initial grid with control points $\mathbf{X}^0$. In the second step, the adjoint problem based on the previously numerical solution, is evaluated. This evaluation computes the sensitivities of the cost function with respect to the different design parameters:

$$\frac{d\mathbf{L}}{d\mathbf{D}} = \left[\frac{\partial \mathbf{L}}{\partial \mathbf{X}} + \frac{\partial \mathbf{L}}{\partial \mathbf{Q}}\frac{\partial \mathbf{Q}}{\partial \mathbf{X}}\right]\frac{d\mathbf{X}}{d\mathbf{D}} \tag{1}$$

where $\frac{d\mathbf{X}}{d\mathbf{D}}$ is the Jacobian matrix. As result, the most sensitive zones of the geometry are detected on the grid points. The gradient of this sensitivity map indicates the movement of the grid points through the control points to obtain an optimized cost function. A complete example of the computational results obtained after this optimization process can be found in [35]. The control points are moved according to the previous step of the optimization process, as a consequence the geometry and mesh are modified and a new iteration is performed until an optimized geometry is obtained.

The comparison between the final geometry of the fin obtained after the optimization process and the original one is shown in Fig. 5. Notice how the shape of the optimized geometry eliminates the sharp corners and smooths the perimeter of the fin. It is also relevant that the bow shows a prominent bulb shape that moves upwards and upstream the high pressure point, which optimizes the aerodynamic performance. It can be seen that the optimized geometry is very similar to the standard fins in height, being the minimum height of the optimized fins in the tip of the leading edge of 0.12 H and the maximum height of 0.22 H at, approximately, the 68% of the fins length.

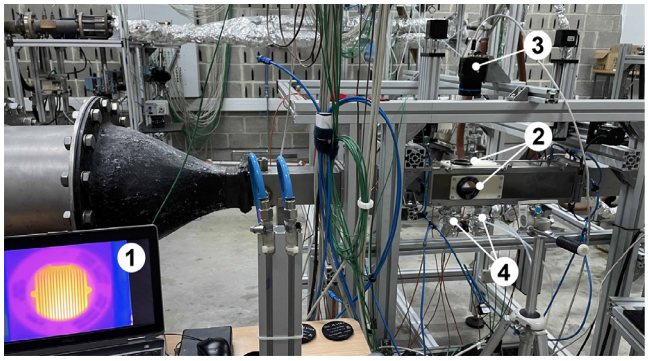

Fig. 6. Infrared measurement setup. (1) Data acquisition, (2) IR windows, (3) thermographic camera, (4) oil system connections.

3.2. Instrumentation

Aerodynamic and thermal data are acquired during the experiments. Pressures are read by GE UNIK 5000 piezoresistive sensors, which were calibrated for the operation regime and present an accuracy of 0.2%. Static pressure is acquired from the piezometric rings and total pressure is acquired by means of 3.2-mm-diameter Kiel probes, which feature a pressure port of Ø 0.82 mm. They are mounted in bi-axial traverse systems that allow a complete characterization of each measurement section.

There are three 2D traverses —for UMS1, DMS1 and DMS2— composed of two stepper motors controlled via MATLAB for synchronization. The main advantage of Kiel probes is that they are insensitive to flow missdirectionality, swirl and turbulence. Nevertheless, since they only measure total pressure, the static pressures from the piezometric rings are considered to compute velocities. Additionally, for a more precise pressure drop measurement between the piezometric rings, a Sensirion SPD2000-L differential pressure sensor with a span of 3000 Pa and a typical accuracy of 1% of the reading is used. The air mass flow is determined by a FOX FT2 mass flow meter of 6″ with a range between 0 and 10,870 Nm^3/hr and an accuracy within ±1% of the reading.

Regarding thermal measurements, the Kiel probes incorporate class 1 T-type thermocouples below the pressure port. However, since the probes are inserted in the tunnel upside-down through openings in the upper wall, the bottom-most region cannot be reached by their thermocouples. This occurs because of the gap that exists between the pressure port at the tip and the thermocouple, when the Kiel is at its lowest height. To characterize the temperature in the lower region, four class 1 K-type grounded thermocouples with 3 mm diameter are used to measure in the Y direction downstream the SACOC. To also characterize the temperature distribution along the SACOC surface, a FLIR A400 thermographic camera set in the range from 0 °C to 120 °C with an accuracy of ±2 °C and a resolution of 320 × 240 pixels is used. Since the field of view through the windows is limited, a complete image can be obtained by combining different snapshots in different positions. This setup is shown in Fig. 6.

In order to characterize the oil flow underneath the SACOC, the oil mass flow is controlled by a KROHNE Optimass 3300C S04 flow meter with a range up to 130 kg/h and an accuracy of ±1% of the actual measured flow rate. To compute the heat exchanged in the process, temperatures at the inlet and outlet are characterize by 4

RTDs: 3 intended to measure the radial distribution and another one inserted co-axially to the pipe, as seen in Fig. 4. Hence, assuming constant heat capacity, the heat transfer is computed by averaging the RTD readings in order to obtain the enthalpy drop:

$$\dot{Q} = \dot{m}\Delta h = \dot{m}c_p\Delta T = \frac{\dot{m}c_p}{4}\left(\sum_{i=1}^{4} T_{\mathrm{in}_i} - \sum_{i=1}^{4} T_{\mathrm{out}_i}\right) \quad (2)$$

3.3. Data acquisition and reduction

The facility setup begins by stating the oil flow through the circuit and heating it up until the desired conditions of mass flow and temperature are reached. Then, the compressor is turned on and air starts flowing through the tunnel; air mass flow is controlled with a series of venting valves. Air and oil conditions need to be modified iteratively until stationary conditions are reached, typically after 20 minutes. The control of all the acquisition systems is centralized using a MATLAB routine, but depending on the measurement, different arrangements are used:

- When performing Kiel probe measurements, each section is measured independently to avoid the influence of upstream probes. Sections are discretized into 400 points in a grid of 20 x 20 and the measurement begins in the uppermost leftmost point (looking in the flow direction). The Kiel probe advances towards the bottom of the tunnel and moves to the next column, beginning the measurement again in the top. Data is acquired through a NI PXI module that reads the voltage from the pressure sensors (Kiel and both piezometric rings), air and oil mass flow meters and temperatures from the reference thermocouples T_{ref} and TC_{Al} (in contact with the SACOC) and the Kiel thermocouple. For each position, a total of 100 samples are taken with a frequency rate of 50 Hz. Each time the probe changes to a new column, the oil temperature in the 8 RTDs is acquired 10 times at a frequency of 1 Hz through an Agilent 34972A data logger.
- For measurements of the wake temperature using the bottom thermocouples downstream the SACOC, special care is put to avoid the sensing tip of each thermocouple being affected by the wake of previous ones, since they all are inserted at the same time, so the thermocouples are placed with 1 mm increments in height. In these tests, 27 points are acquired in the central ($Z = 0$) plane and, for each point, three readings are made during 45 seconds with the same data rates as previously mentioned for both PXI and data logger of 50 and 1 Hz respectively.
- Regarding the pressure drop tests, these are carried out varying the air mass flow until stationary conditions are reached. Then, the acquisition is performed reading the air mass flow, reference temperature and differential pressure between the inlet and outlet piezometric rings with a data rate of 25 Hz during one minute. Since it has been observed that the addition of heat does not modify the pressure drop results, all tests were done without the oil system.
- Finally, for the thermographic measurements, the camera is set in position focusing on a specific region of the SACOC and when stationary conditions are reached, air mass flow and the reference temperature are acquired together at 50 Hz during one minute, ensuring that the position of the reference thermocouple TC_{Al} is within the field of view of the camera snapshot, to facilitate the calibration. A total number of 8 readings is made for each camera position.

Regarding data reduction, since the readings are made in stationary conditions, the values are averaged from the data set. In terms of Kiel measurements and the wake temperature characterization, several acquisitions are performed in different days. Additionally, for the measurements in which the air temperature is analyzed, the temperatures are corrected using the reference temperature T_∞ measured upstream of the wind tunnel, shown in Fig. 3. This is due to the fact that a perfectly thermal stationary state takes several hours to be obtained because of the thermal inertia of the facility. Hence, the average reference temperature during the test is used to correct the air temperatures measured in the test section, thereby correcting the slight temperature drift of the facility.

4. Results and discussion

4.1. Aerodynamic performance

Although the main purpose of a heat exchanger is to evacuate as much temperature as possible from the hot source, in this particular application it is required to do so without heavily impacting the aerodynamics in the air side, since this exchanger is using the bypass airflow as cold sink, and this airstream will then be expanded in the secondary nozzle to obtain thrust. Thus, the characterization of the pressure and velocity field, together with the pressure drop induced by the SACOC is studied in this section.

Firstly, velocity is derived from the Kiel total pressure and temperature data, and the static pressure measured through the piezometric rings, by applying the standard isentropic flow relations. Interpolated velocity contours are analyzed in Fig. 7, where each row represents the contours in the same section for the different SACOC versions and each column displays the velocity evolution along the sections for one version. As expected, velocity at UMS1 shows almost identical contours with an horizontal distribution matching the target profile. The baseline geometry, being a flat plate, presents very similar results for all sections, slightly decreasing the gradients in the downstream direction.

The standard and optimized geometries show similar behaviours, with a strong impact of the fins at DMS1, lowering considerably the velocity. In both cases, there is a zone close to the bottom with specially low values and a transition phase to the freestream conditions. This zone seems to be smaller in the case of the optimized fins. The downstream-most section, DMS2, is also influenced by the SACOC fins, but the region of influence is not as defined as in DMS1, spreading towards the lateral walls and regaining speed. The lateral zones of the test section, which are not behind the fins, experience an acceleration up to the same height approximately equal to that observed for the wake. This increase in velocity is also higher in the DMS1.

For a more detailed analysis, velocity profiles are displayed in Fig. 8. These represent the averaged values of the center region $Z \in (-0.25H, +0.25H)$, which is the SACOC span. This averaging is done to avoid displaying only the effect of the particular fin/channel at the center. Error bars displayed in the figure represent the standard deviation in the mean values after several measurements. For the UMS1, the velocity profiles are almost identical and the downstream sections present the same velocity profiles above the 25–30% of the section. This means that the influence of the fins is limited to a region only very slightly higher than themselves. While the top wall of the tunnel develops a certain boundary layer, above the 75% of H (absent in the bypass at this height), it can be seen that this boundary layer does not interact with the area influenced by the SACOC, thereby validating the approach of a limited height wind tunnel.

The velocity profile of the baseline model varies only very slightly from one plane to another, this is, the effect of the distortion screen is well kept along the tunnel. Both cases with fins, standard and optimized, reproduce a very similar pattern with a

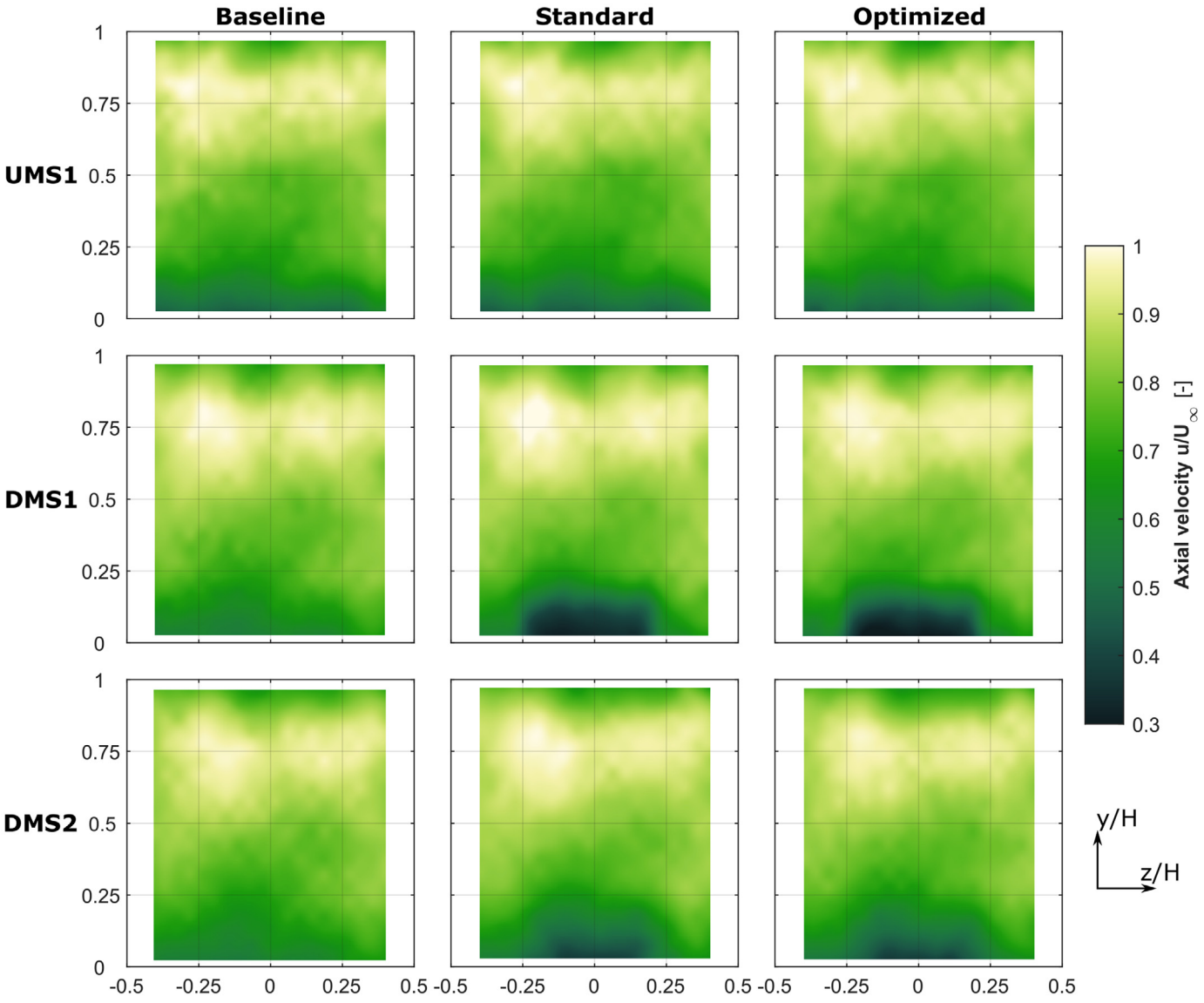

Fig. 7. Velocity contours comparison for the different SACOC geometries (columns) measured at UMS1, DMS1 and DMS2 (rows) with a typical measurement uncertainty of ±0.06. Note specially the clear 'velocity sink' that appears in the wake of the finned versions.

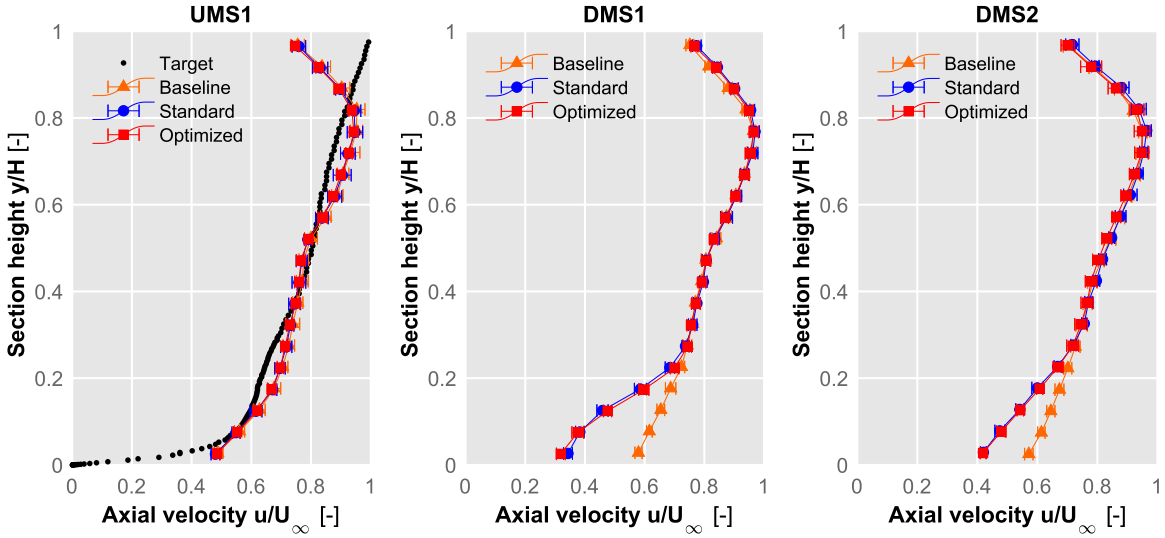

Fig. 8. Velocity profiles averaged in the center region $Z \in (-0.25H, +0.25H)$ for the different SACOC geometries at each section with a typical measurement uncertainty of ±0.06.

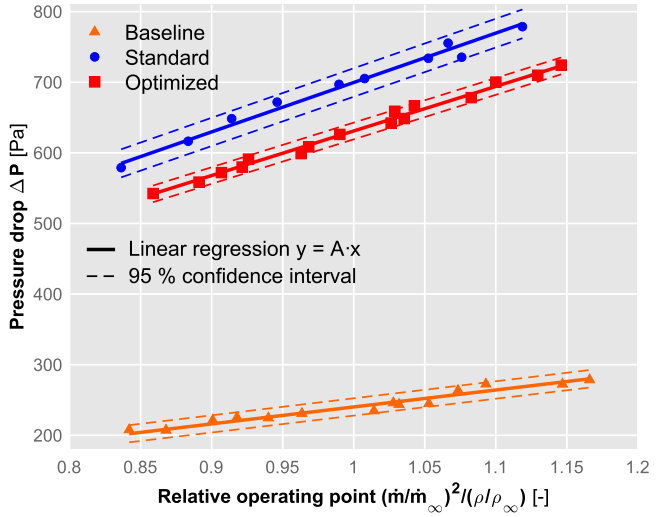

Fig. 9. Pressure drop variation with $\dot{m}^2/\rho$ for each geometry with a typical measurement uncertainty of ±1%.

region of lower velocities downstream the SACOC due to the wake produced by the fins. This wake is stronger at DMS1 and diffuses into a larger region as the flow advances to DMS2.

In terms of turbulence intensity, the presence of the distortion panel generates not only a certain velocity distribution, but a turbulent intensity distribution too: the region with lower velocities (lower porosity in the panel) experiences higher levels of turbulence, being the turbulence intensity levels below 3% for the top 3/4 of the height (as measured by a high-frequency pitot probe), and increasing gradually up to 7% in the lower part of the tunnel. After the SACOC, the values in the upper region remain approximately the same until a third of the height, where the presence of the wake increases the values. This increment persists at DMS2.

Regarding the pressure drop induced by the exchanger in the air side, Fig. 9 shows the pressure drop for each version under different mass flows conditions. For an incompressible flow the pressure drop can be written [26] as:

$$\Delta p = K\frac{1}{2}\rho U^2 \tag{3}$$

Where ρ is the density, U the velocity magnitude and K is a pressure drop coefficient that should only be dependent on the Reynolds number, and for high enough Re values, essentially constant. By recalling the continuity equation $\dot{m} = \rho A U$, this can be rearranged as:

$$\Delta p = \frac{K}{2A^2}\frac{\dot{m}^2}{\rho} \tag{4}$$

And so Δp should be essentially linearly dependent on $\dot{m}^2/\rho$. As seen in Fig. 9, this is the case for all three configurations at the considered mass flow range, around ±15% of the nominal flow. The main advantage of this fact is that therefore, the pressure drop for each configuration is characterized by a constant K and the losses can be readily computed for different air mass flow settings.

As expected, the pressure drop induced by the flat plate is much lower than that caused by the fins. However, even though they present a very similar velocity distribution, the pressure drop associated to the optimized versions of the fins is lower than that of the standard fins, achieving almost a 10% reduction in pressure drop under nominal conditions, therefore validating the numerical optimization procedure. This can be explained by the difference in the aerodynamic interaction of both geometries with the flow, that has been deeply analysed in [35]. The optimized geometry presents considerably lower turbulent kinetic energy values in the wake and almost no vortical structures on the tip of the fins are formed, compared to the geometry with standard fins.

4.2. Aerothermal performance

In terms of heat exchange, temperatures were measured on both sides, air and oil. The reference temperature T_∞ was measured with a thermocouple inserted in the S-duct upstream the settling chamber (see Fig. 3). For the air side, interpolated temperature contours from the thermocouples in the Kiel probes are shown in Fig. 10. Since the lower 12% of the section is not reached by the Kiel thermocouple, there is a gap in the contours at the bottom. The figure shows that temperature only increases in the region close to the fins: above the 30% of the channel height the temperature remained almost constant, whereas for the bottom part, the temperature increases as it approaches the bottom.

The influence of the fins is not appreciated close to the lateral walls, since the most heated part of the air is propagated along with the wake, being precisely the region seen in Fig. 7 affected in velocity the one affected by the temperature increase. In the case of the baseline, the temperature increase is weaker and limited to lower regions, so it is not captured by the thermocouple in the probes. For the standard and optimized version, mainly in the latest, there is an increase in temperature that follows the finned pattern.

For a more detailed analysis of the temperature along the exchanger wake, Fig. 11 shows the results from the four wake thermocouples. Again, the finned geometries present more similar values than the first version, although the three of them follow a similar trend. The maximum is reached at 3–4% of the height and decreases continuously to the ambient temperature at a height between 25 and 30% of the channel section. Note that since the reference temperature T_∞ is measured well upstream the SACOC, the freestream temperature will be slightly lower at the TC1-4 positions due to the heat losses across the wind tunnel, leading to very slightly negative T/T_∞ values in Fig. 11.

As they get further from the SACOC, maximum values decrease and the temperature descent towards the top is smoother. Values between the maximum and the tunnel floor decrease since the floor absorbs part of the heat present in the wake as it is made of steel. Another aspect worth considering is the fact that temperatures in the optimized version are higher than those for the standard case, especially in the regions closer to the exchanger.

In order to obtain a more complete picture of the thermal performance, the temperature distribution on the aluminium base was measured with a thermographic camera. As mentioned, in order to achieve proper results, IR windows transparent in the long wave infrared (LWIR) were installed facing the exchanger, and the SACOC and its surroundings were painted with a specific graphite-based black paint for homogeneous emissivity. A calibration for the temperature ranges was performed and to double-check the results obtained, the temperature was also measured with the aforementioned TCAl thermocouple inserted through one of the stubs used to attach the SACOC to the oil pan. Additionally, the region over the TC1 insert was also painted. Since the available field of view is not enough to capture the whole surface, a composition has been done with four different snapshots.

Figure 12 represents on the top plot the temperature evolution along the base center line ($z = 0$) from each one of the versions. The bottom part of the figure depicts a thermal image composition for each different SACOC version as seen from above. The composed images are aligned with the graphic, with vertical dashed lines indicating the leading and trailing edges of the fins, and with horizontal dashed lines representing from where the data from the

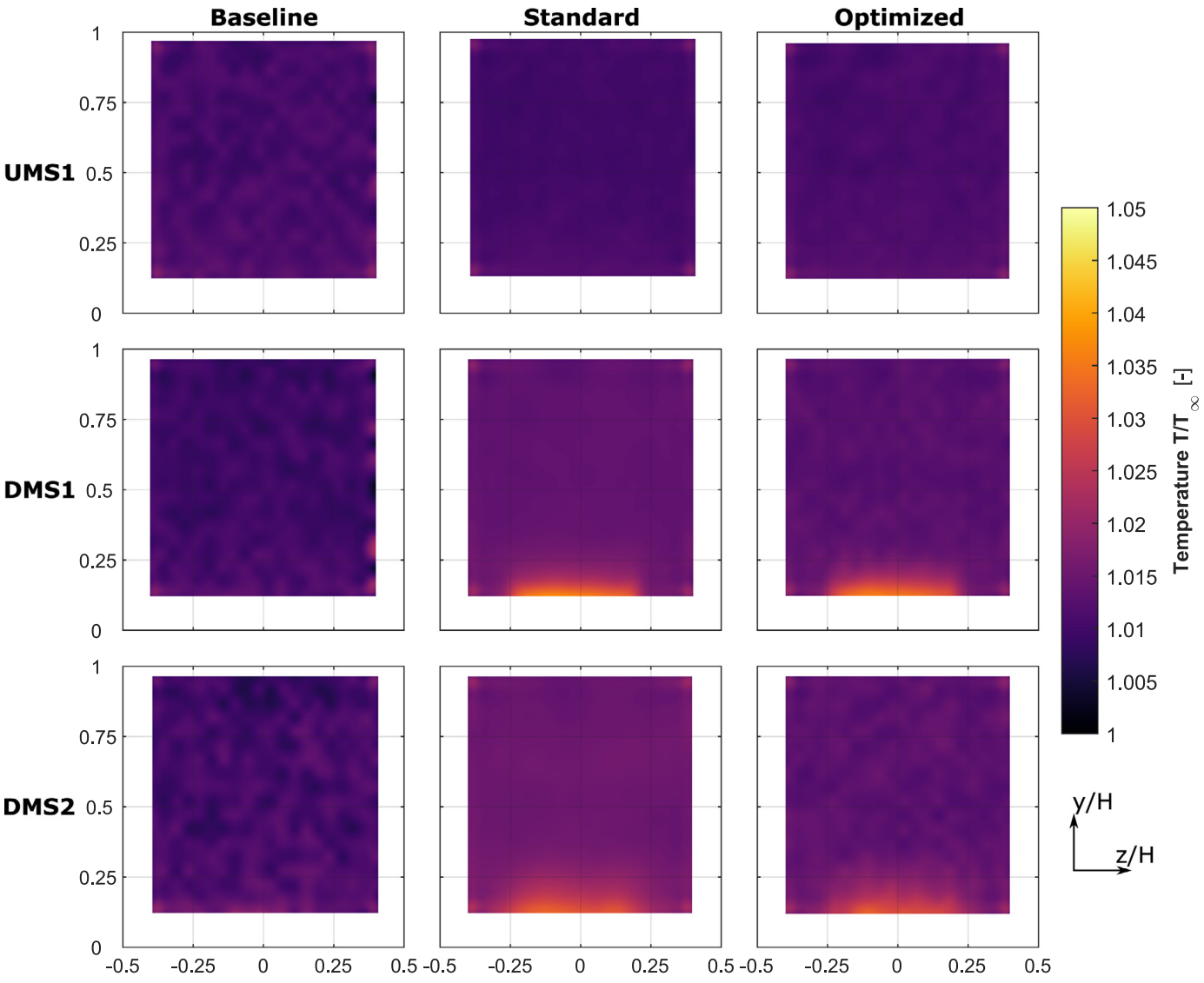

Fig. 10. Total temperature contours comparison for the three SACOC geometries (columns) measured at UMS1, DMS1 and DMS2 (rows) with a typical measurement uncertainty of ±0.004.

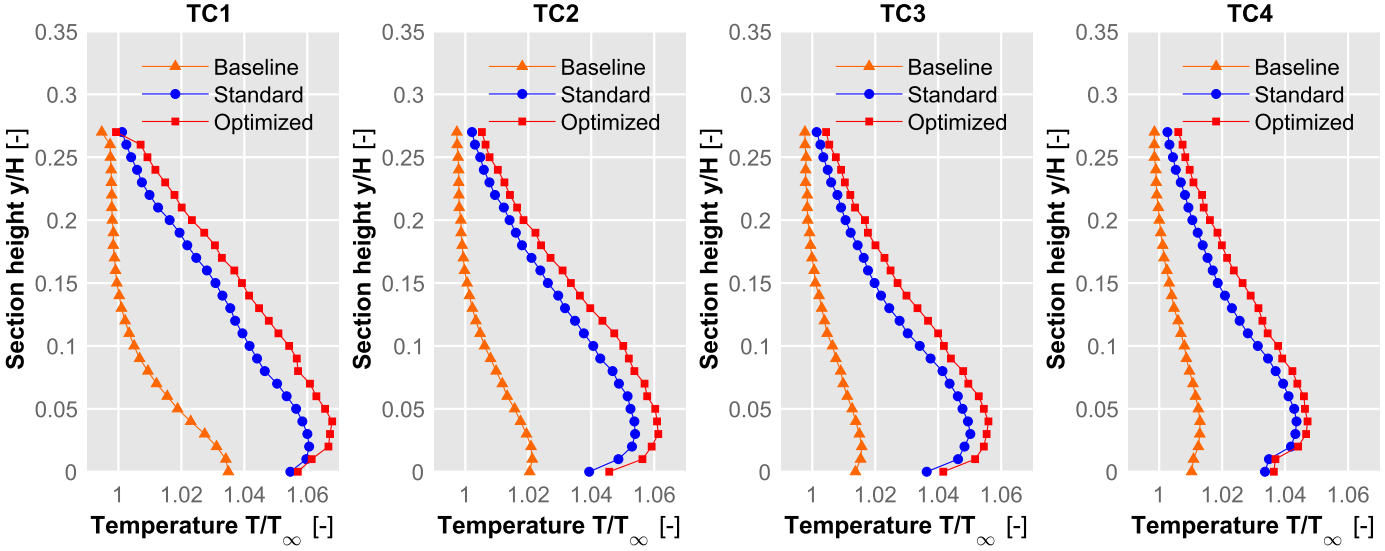

Fig. 11. Wake temperature profiles for the different geometries as measured by the thermocouple array downstream the SACOC with a typical measurement uncertainty of ±0.005.

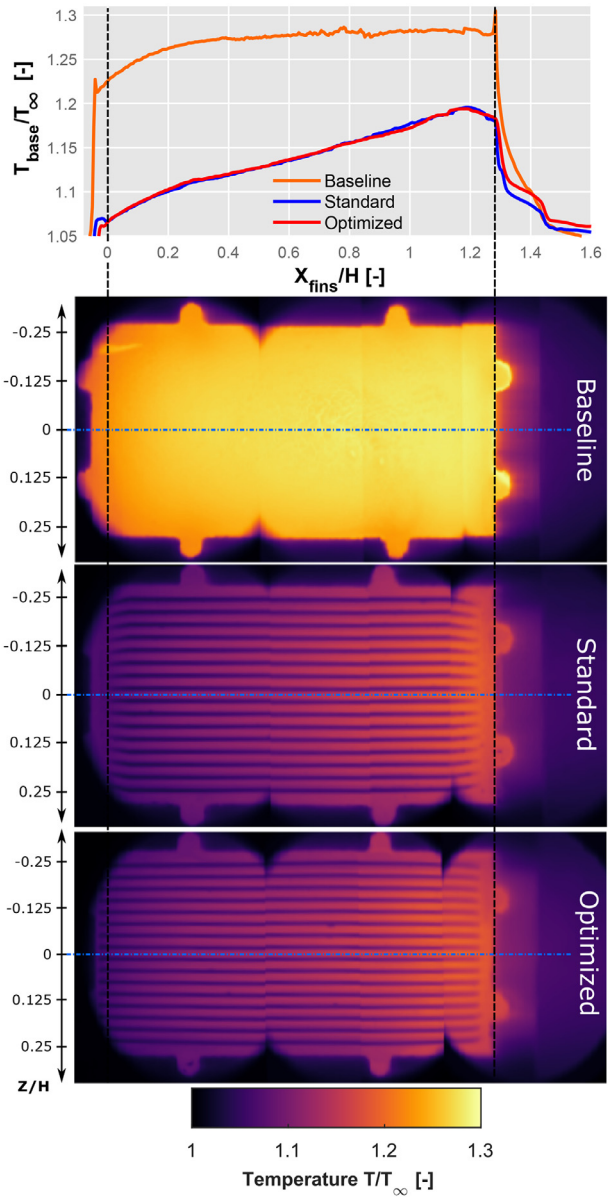

Fig. 12. Temperature evolution of the heat exchanger base along the center line (top plot) and surface temperature distribution (bottom plots) for each geometry with a typical measurement uncertainty of ±0.008.

top plot is extracted. Note that the baseline leading edge is assumed to be at the same location as in the other cases, this is, at the bottom leading edge of the fins.

As it can be seen, the baseline presents much higher temperatures than the other versions, reaching almost a constant temperature halfway the end of the exchanger. The finned versions, on the other hand, experience a continuous increase of the base temperature up to the end. That occurs due to the continuous heating the air experiences while going through the exchanger. Besides, a non-negligible fraction of the mass flow rate that runs through the fins may have escaped by the upper side of the SACOC by the time it reaches the trailing edge [25]. Therefore, heat exchange is degraded near the trailing edge and the base temperature is higher. For both versions, the temperature evolution along the base is almost identical.

As expected, the hotter zone in the finned versions is way cooler than in the flat plate, highlighting the effect of the fins. It is interesting to notice the effect of the oil pan insulation, that drastically reduces the temperature around the SACOC, preventing conductive heat losses to the wind tunnel floor. Finally, the temperatures in the floor induced by the wake also show the same behaviour as the TC1 thermocouple: higher temperature for the optimized fins, followed close by the standard geometry and lower one in the baseline. This difference in temperature for the finned versions, which present almost identical base temperature distribution, might be explained by the difference in the temperature distribution along the fin height. Although it has not been captured experimentally, the different fin temperature distributions can be observed in the previous computational study performed by Chávez-Modena et al. [35].

In the oil side, the fluid enters the oil pan with an average temperature of 1.33 T_∞ at a mean flow rate of $18.1 \times 10^{-3} \dot{m}_\infty$, and advances below the SACOC in a laminar regime. The variation of these values together with the air conditions, was less than 1% among the cases. After leaving the heat exchanger, the temperature of the oil was reduced 1.115% for the baseline, 2.936% for the standard fins and 3.234% for the optimized ones. Compared with the baseline heat exchange $\dot{Q}_b$, this means a heat evacuation of 2.66 ± 0.03 $\dot{Q}_b$ and 2.9 ± 0.03 $\dot{Q}_b$ for the standard and optimized geometries, respectively. In general, it can be said that the addition of fins is an adequate choice in this case, since the use of fins is considered justified when their effectiveness approximately doubles the heat removed without them [34].

It is confirmed that the geometry with more heat extraction is the optimized one, not only presenting lower pressure drop but also reducing to lower values the oil temperature. As previously explained, this is caused by an increment in the fin surface, which enables it to evacuate more heat, but in such a way that the geometry impact on the air flow is smoother than the case with standard fins.

However, as previously stated, the heat extraction capacity is not the most important feature to improve in these types of heat exchangers, but their permeability to the flow. Since the goal is to maintain the heat exchange constant (as it is an operability parameter) and reduce the pressure drop, a possible consideration is to reduce the size of the fins. With this, both values would decrease: the heat would return to its nominal value and the pressure drop would also diminish, improving the performance of the SACOC.

4.3. Effect of the velocity profile

In order to assess the effect of the realistic velocity profile —which is one of the main features of the experimental setup— in the aerothermal performance of the SACOC, measurements were taken with and without the distortion screen at the same mass flow. To this end, only the geometry with standard fins is analyzed.

Fig. 13 represents the central velocity profiles for both cases, with and without the distortion screen, being the one called *Clean* the one without the panel. The velocity profile is quite uniform in the first plane for the clean and the downstream sections show the influence of the wake in a very similar manner as in the case with the distortion screen. However, since the velocity in the bottom part at UMS1 is larger, it has higher values in the wake too.

Above the 30% of the section, the velocity profile reaches again free flow conditions, but with higher values than those in the same region at UMS1, due to the deceleration in the bottom part caused by the wake.

In terms of pressure drop, the clean configuration presents an increase in the value of 9.82% in comparison with the case with the distortion screen, since values for the nominal conditions go up to 772 Pa. The explanation for this could lie on the fact that the fins are the feature in the test section that affects the pressure drop the most, so, by having larger velocities in that part of the tunnel, the pressure drop rises.

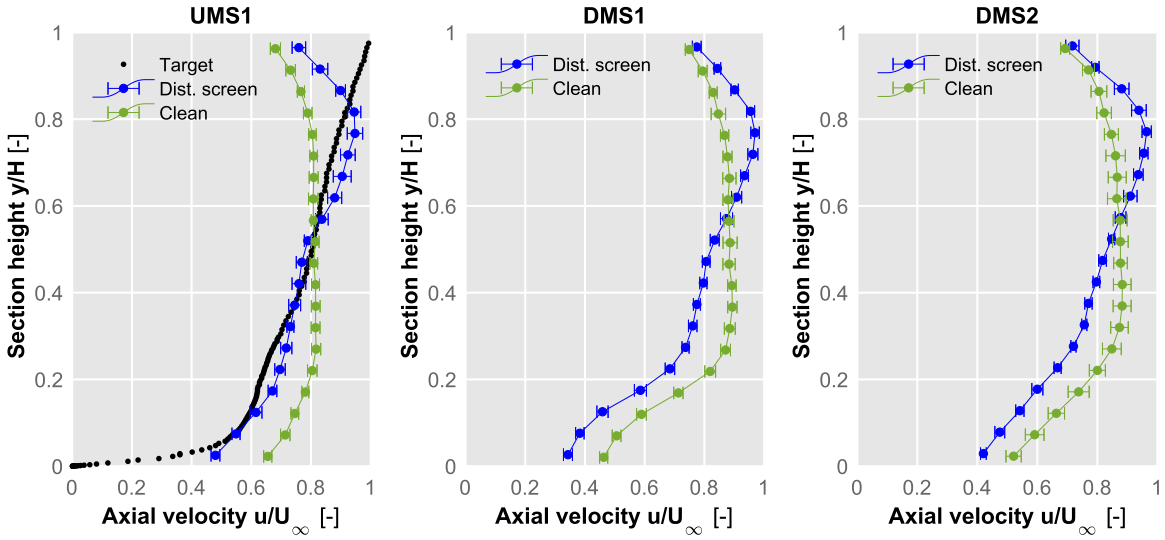

Fig. 13. Velocity profiles averaged in the center region $Z \in (-0.25H, +0.25H)$ for the standard fins geometry with and without distortion screen with a typical measurement uncertainty of ±0.06.

Regarding the heat exchange, the absence of the distortion screen raises the heat transfer to $3 \pm 0.035\ \dot{Q}_b$, which represents an increase of 10.74% compared to the case with the same geometry but incorporating the distortion panel. In this case, a higher mass flow of air in the fins region is beneficial to extract a larger amount of heat from the oil.

With these results, it is important to note that in order to perform aerothermal studies reducing the height in the region of interest, a modification of the velocity profile is required in order to match the actual flow conditions. This confirms the conclusion reached by Gelain et al. [25] using numerical means.

4.4. Summary

Three different geometries have been analyzed to determine the impact on the performances of a heat exchanger. Indeed, the pressure drop induced and the heat release achieved are the main parameters to consider in most exchangers. In order to compare the different cases, two typical parameters are utilized: the Fanning friction factor f and the overall heat transfer coefficient U. The former is related to the pressure drop in the following manner:

$$f = \frac{\Delta p}{2L} \frac{D_h}{v^2 \rho} \tag{5}$$

being Δp, L, D_h, v and ρ the pressure drop, length of the heat exchanger, section hydraulic diameter, flow velocity and density, respectively.

The overall heat transfer coefficient U estimates the capability of a heat exchanger to extract the energy from the hot source in a determined area. In a counter-flow heat exchanger, it is defined [34] as:

$$\dot{Q} = UA\Delta T_{\text{lm}} = UA \frac{\Delta T_1 - \Delta T_2}{\ln\left(\frac{\Delta T_1}{\Delta T_2}\right)} \tag{6}$$

where A is the area of the exchanger, ΔT_{lm} is the *log-mean* temperature difference and ΔT_1 and ΔT_2 are defined in the SACOC as $\Delta T_1 = T_{\text{oil in}} - T_{\text{air out}}$ and $\Delta T_2 = T_{\text{oil out}} - T_{\text{air in}}$. By estimating $T_{\text{air out}}$ through a heat addition $\dot{Q}$ (obtained from Eq. (2) assuming no further losses) we can solve Eq. (6) for U.

Table 2 summarizes the results obtained with the different geometries in terms of Fanning friction f factor and overall heat transfer coefficient U, considering the rectangular base area as reference surface.

Table 2
Fanning friction factor f and overall heat transfer coefficient U of the three geometries at nominal conditions.

Geometry	$f \times 10^3$ [-]	U [W/(m^{2}K)]
Baseline	8.26 ± 0.092	314.08 ± 7.72
Standard	24.09 ± 0.266	896.02 ± 18.33
Optimized	21.69 ± 0.239	942.88 ± 18.92

As expected, the Fanning factor increases considerably in the finned exchangers, but so does the heat transfer coefficient. It is interesting to notice how they increase in a very similar proportion for the standard configuration, suffering even the friction factor a slight higher increase, whereas, for the optimized fins, the increase in heat transfer capability exceeds the increment in the Fanning factor.

5. Conclusions

Surface air-cooled oil cooler devices are a solution with high potential to successfully tackle the thermal challenges brought by new turbofans generations. However, as they utilize an air stream the main purpose of which is to generate propulsion, it is crucial to implement this solution in such a way that the impact on the propulsive efficiency is as low as possible.

In this investigation, the experimental approach of considering a smaller region around the fins for more affordable tests has been validated. The influence of the fins in the downstream sections is relegated to the bottom 20–30% of the section (being the fins a 20% of the tunnel height) and the profile above that value is identical to a baseline case with no fins.

Nevertheless, in order to successfully apply this approach it is crucial to replicate an adequate velocity distribution to study the actual exchanger performances under realistic conditions. In order to do so, the usage of a distortion screen that replicates the velocity profile in the surroundings of the SACOC has been demonstrated to be of high importance.

Using this setup, an experimental characterization of the aerothermal performances of different geometries has been carried out. Specifically, three versions have been analyzed: a baseline, which a simple flat plate; standard fins, which incorporates a series of trapezoidal fins; and optimized fins, which is the result of a topological optimization of the standard fins shape. In terms of ve-

locities and temperatures, the three versions exhibit almost identical values for regions above the 30% the tunnel height. Regarding pressure drop and heat exchange, a summary of the results can be seen in Table 2 in forms of Fanning friction factor and overall heat transfer coefficient.

Although adding fins with a standard geometry to a flat plate increases considerably the heat exchanged, it rises the pressure drop induced in the air side. Nevertheless, it has been demonstrated how a topologically optimized geometry obtained through numerical simulations can achieve a significant reduction in pressure drop and an increase in heat exchange compared to the regular fins.

This result highlights the importance of both numerical twins able to support numerical optimizations and the corresponding experimental methodologies, such as the one presented in this work, able to both gather the required inputs for building the numerical model and later validate the aerothermal performance of the resulting SACOC geometries.

In conclusion, it is becoming fundamental for engine manufacturers to evaluate the performance of heat exchangers in small scale tests. Ideally, full engine tests would always be performed, but they are extremely expensive, time consuming and not always easy to exploit. Smaller, scaled experimental methodologies such as the one proposed in this work allow instead to test numerous geometries and flow conditions while reducing dramatically the use of resources compared with full engine tests.

Declaration of Competing Interest

The authors declare that they have no known competing financial interests or personal relationships that could have appeared to influence the work reported in this paper.

CRediT authorship contribution statement

A. Broatch: Conceptualization, Methodology, Supervision, Project administration, Funding acquisition. **P. Olmeda:** Conceptualization, Methodology, Formal analysis. **J. García-Tíscar:** Methodology, Investigation, Visualization, Writing – original draft. **A. Felgueroso:** Investigation, Data curation, Visualization, Writing – original draft. **M. Chávez-Modena:** Methodology, Software, Validation. **L.M. González:** Methodology, Software, Validation, Writing – original draft. **M. Gelain:** Conceptualization, Methodology, Resources, Supervision, Writing – review & editing. **A. Couilleaux:** Conceptualization, Methodology, Resources, Supervision.

Acknowledgments

This project has received funding from the Clean Sky 2 Joint Undertaking under the European Union's Horizon 2020 research and innovation programme under grant agreement n° 831977: *Aerodynamic upgrade of Surface Air-Cooled Oil Coolers (SACOC)*. A. Felgueroso is supported through the Programa de Apoyo para la Investigación y Desarrollo of the Universitat Politècnica de València under grant PAID-01-20 n° 21589. The authors also wish to thank Safran Aircraft Engines for their kind permission to share the data presented in this publication. Special thanks are also given to Mr. Adolfo Guzmán for his inestimable support during the experimental campaign.

References

[1] J.-F. Brouckaert, F. Mirville, K. Phuah, P. Taferner, Clean sky research and demonstration programmes for next-generation aircraft engines, The Aeronautical Journal 122 (1254) (2018) 1163–1175, doi:10.1017/aer.2018.37.
[2] IATA, Aircraft Technology Roadmap to 2050, 2019.
[3] K. Hart, Basic architecture and sizing of commercial aircraft gas turbine oil feed systems, in: Volume 4: Heat Transfer, Parts A and B, ASMEDC, 2008, pp. 1431–1441, doi:10.1115/GT2008-50450.
[4] P. Gloeckner, C. Rodway, The evolution of reliability and efficiency of aerospace bearing systems, Engineering 09 (11) (2017) 962–991, doi:10.4236/eng.2017.911058.
[5] A.S. van Heerden, D.M. Judt, C.P. Lawson, S. Jafari, T. Nikolaidis, D. Bosak, Framework for integrated dynamic thermal simulation of future civil transport aircraft, AIAA Scitech 2020 Forum, American Institute of Aeronautics and Astronautics, 2020, doi:10.2514/6.2020-1942.
[6] W.J. Vankan, R. Maas, V. Peyron, Optimisation methodology for integrated equipment installation in new engine architecture nacelles, Proceedings of the Institution of Mechanical Engineers, Part G: Journal of Aerospace Engineering (2019), doi:10.1177/0954410019895883. 095441001989588
[7] Q. Li, G. Flamant, X. Yuan, P. Neveu, L. Luo, Compact heat exchangers: a review and future applications for a new generation of high temperature solar receivers, Renewable Sustainable Energy Rev. 15 (9) (2011) 4855–4875, doi:10.1016/j.rser.2011.07.066.
[8] X. Zheng, Z. Qi, A comprehensive review of offset strip fin and its applications, Appl Therm Eng 139 (2018) 61–75, doi:10.1016/j.applthermaleng.2018.04.101.
[9] R. Krupiczka, A. Rotkegel, H. Walczyk, L. Dobner, An experimental study of convective heat transfer from extruded type helical finned tubes, Chem. Eng. Process. 42 (1) (2003) 29–38, doi:10.1016/S0255-2701(02)00014-4.
[10] M.K. Aliabadi, F. Hormozi, Performance analysis of plate-fin heat exchangers: different fin configurations and coolants, J. Thermophys Heat Transfer 27 (3) (2013) 515–525, doi:10.2514/1.T4041.
[11] Steve G. Mackin, Samuel J. Tutko, Bleed Air Boosted Engine Oil Cooler, 2020.
[12] Adrien Louis Simon, Jean-Charles Michelle Pierre Di Giovanni, Boris Pierre Marcell Morelli, Lubricating and cooling core for a mechanical reduction gear of an aircraft turbofan engine, 2020.
[13] T. Filburn, A. Kloter, D. Cloud, Design of a carbon-carbon finned surface heat exchanger for a high-bypass ratio, high speed gas turbine engine, in: Volume 3: Heat Transfer, Parts A and B, ASMEDC, 2006, pp. 483–490, doi:10.1115/GT2006-90480.
[14] M. Williams, A. Muley, J. Bolla, H. Strumpf, Advanced heat exchanger technology for aerospace applications, Advanced Heat Exchanger Technology for Aerospace Applications, 2008, doi:10.4271/2008-01-2903.
[15] D. Saltzman, M. Bichnevicius, S. Lynch, T.W. Simpson, E.W. Reutzel, C. Dickman, R. Martukanitz, Design and evaluation of an additively manufactured aircraft heat exchanger, Appl Therm Eng 138 (2018) 254–263, doi:10.1016/j.applthermaleng.2018.04.032.
[16] P. Dube, S. Hiravennavar, A. Ali Z, Statistical model to predict air side pressure drop for heat exchangers, Statistical Model to Predict Air Side Pressure Drop for Heat Exchangers, 2018, doi:10.4271/2018-01-0081.
[17] M. Bošnjaković, S. Muhič, A. Čikić, Experimental testing of the heat exchanger with star-shaped fins, Int J Heat Mass Transf 149 (2019), doi:10.1016/j.ijheatmasstransfer.2019.119190.
[18] H. Zhang, J. Guo, X. Cui, J. Zhou, X. Huai, H. Zhang, K. Cheng, Z. Han, Experimental and numerical investigations of thermal-hydraulic characteristics in a novel airfoil fin heat exchanger, Int J Heat Mass Transf 175 (2021), doi:10.1016/j.ijheatmasstransfer.2021.121333.
[19] J. Gong, J. Onishi, A. He, Y. Kametani, Y. Hasegawa, N. Shikazono, Heat transfer enhancement and pressure loss in a plate-fin heat exchanger with v-shaped oblique wavy surface, Int J Heat Mass Transf 161 (2020), doi:10.1016/j.ijheatmasstransfer.2020.120263.
[20] L. Zhang, Z. Qian, J. Deng, Y. Yin, Fluid-structure interaction numerical simulation of thermal performance and mechanical property on plate-fins heat exchanger, Heat Mass Transfer 51 (9) (2015) 1337–1353, doi:10.1007/s00231-015-1507-5.
[21] S. Kim, J.K. Min, M.Y. Ha, C. Son, Investigation of high-speed bypass effect on the performance of the surface air-oil heat exchanger for an aero engine, Int J Heat Mass Transf 77 (2014) 321–334, doi:10.1016/j.ijheatmasstransfer.2014.05.025.
[22] M. Kim, M.Y. Ha, J.K. Min, A numerical study on various pin-fin shaped surface air-oil heat exchangers for an aero gas-turbine engine, Int J Heat Mass Transf 93 (2016) 637–652, doi:10.1016/j.ijheatmasstransfer.2015.10.035.
[23] L. Villafañe, G. Paniagua, Aerodynamic impact of finned heat exchangers on transonic flows, Exp. Therm Fluid Sci. 97 (2018) 223–236, doi:10.1016/j.expthermflusci.2018.04.012.
[24] J. Sousa, L. Villafañe, G. Paniagua, Thermal analysis and modeling of surface heat exchangers operating in the transonic regime, Energy 64 (2014) 961–969, doi:10.1016/j.energy.2013.11.032.
[25] M.C. Gelain, A. Couilleaux, M. Errera, R. Vicquelin, O. Gicquel, Conjugate heat transfer analysis of a surface air-cooled oil cooler (SACOC) installed in a turbofan by-pass duct, in: AIAA AVIATION 2021 FORUM, American Institute of Aeronautics and Astronautics, 2021, p. 22, doi:10.2514/6.2021-3163.
[26] A. Torregrosa, A. Broatch, J. García-Tíscar, F. Roig, Experimental verification of hydrodynamic similarity in hot flows, Exp. Therm Fluid Sci. 119 (2020) 110220, doi:10.1016/j.expthermflusci.2020.110220.
[27] J.R. Serrano, F.J. Arnau, L.M. Gracía-Cuevas, V. Samala, L. Smith, Experimental approach for the characterization and performance analysis of twin entry radial-inflow turbines in a gas stand and with different flow admission conditions, Appl Therm Eng 159 (2019) 113737, doi:10.1016/j.applthermaleng.2019.113737.
[28] J.R. Serrano, F.J. Arnau, L.M. García-Cuevas, P. Soler, R. Cheung, Experimental validation of a one-dimensional twin-entry radial turbine model

under non-linear pulse conditions, Int. J. Engine Res. (2019), doi:10.1177/1468087419869157. 1468087419869157.
[29] Community Research and Development Information Service, Novel system removes debris from compressor, Research*eu results magazine 50 (2016) 22.
[30] M. Chavez-Modena, L.M. González, E. Valero, A. Broatch, J. García-Tíscar, A. Felgueroso, Numerical and experimental analysis of thermo-aerodynamic performance in an aero engine surface heat exchanger, in: AIAA AVIATION 2021 FORUM, 2021, p. 12, doi:10.2514/6.2021-2901.
[31] G. Paniagua, D. Cuadrado, J. Saavedra, V. Andreoli, T. Meyer, J.P. Solano, R. Herrero, S. Meyer, D. Lawrence, Design of the purdue experimental turbine aerothermal laboratory for optical and surface aerothermal measurements, J Eng Gas Turbine Power 141 (1) (2018), doi:10.1115/1.4040683.
[32] Alcoa Global Cold Finished Products, Characteristics of Aluminium 7075, 2021.
[33] Ultem 1010 properties, 2021, Accessed: 2021-05-26 (https://www.stratasys.com/es/materials/search/ultem1010).
[34] F.P. Incropera, Fundamentals of Heat and Mass Transfer, 6th ed, John Wiley, Hoboken, NJ, 2007.
[35] M. Chavez-Modena, L.M. González, E. Valero, Numerical optimization of the fin shape experiments of a heat conjugate problem surface air/oil heat exchanger (SACOC), Int J Heat Mass Transf 182 (2021) 121971, doi:10.1016/j.ijheatmasstransfer.2021.121971.
[36] F. Giannetti, P. Luchini, Structural sensitivity of the first instability of the cylinder wake, J Fluid Mech 581 (1) (2007) 167–197, doi:10.1017/S0022112007005654.
[37] P. Luchini, A. Bottaro, Adjoint equations in stability analysis, Annu Rev Fluid Mech 46 (2014) 493–517, doi:10.1146/annurev-fluid-010313-141253.